Mathematical Model of Scrap Melting in EAF using Electromagnetic Stirring

Niloofar Arzpeyma[1], Ola Widlund[2], Mikael Ersson[1], Pär Jönsson[1]*

[1)] *Department of Materials Science and Engineering, Royal Institute of Technology (KTH), SE-100 44, Stockholm, Sweden.*

[2)] *ABB AB, Corporate Research, SE-721 78, Västerås, Sweden*

Abstract: The influence of electromagnetic stirring on melting of a single piece of scrap in an eccentric bottom tapping (EBT) electric arc furnace (EAF) was studied numerically. A mathematical model was developed to study the heat transfer and fluid flow in the melt for conditions both with and without electromagnetic stirring. The source terms for momentum transfer were electromagnetic and buoyancy forces, and the only source term considered in the energy conservation equation was the arc power. A finite element method (FEM) based software VectorFields OPERA was used to add electromagnetic forces to the momentum equation, and a finite volume method (FVM) based software FLUENT was used to solve momentum conservation, continuity and energy conservation equations inside the melt. The slag is modeled explicitly as a solid wall with high thermal conductivity. The enthalpy-porosity technique was applied to track the phase change of a scrap piece defined in the EBT region of the furnace. The model was applied for different scrap sizes, preheating temperatures, stirring directions and force magnitudes. The predicted heat transfer rate at the melt-scrap interface was used to estimate the heat transfer coefficient. It was seen that the electromagnetic stirring is a viable way to improve the melting capability of the EAF.

Keywords: EAF, Electric Arc Furnace, Mathematical Model, CFD, Electromagnetic Stirring

1. Introduction

Today, electric arc furnaces (EAFs) are operating with significantly reduced tap–to–tap time and energy consumption compared to 30 years ago; however, understanding of the melting process in EAF is still of interest to contribute to further improvements in productivity and energy efficiency in the steelmaking industry. The melting process of scrap metals has been studied by considering scrap size, shape and preheating temperature, melt temperature and melt stirring by using both experiments and numerical modeling.

Guthrie et al. [1] used a finite difference method to solve the equation for unsteady heat conduction through a sphere to study melting of iron scraps in a stagnant melt.

It was shown that natural convection generated around the scrap surface, having lower temperature, leads to a lower melting time than the condition the melt is completely stagnant. The heat transfer coefficient was calculated using a Nusselt number correlation for natural convection from horizontal cylinders to fluids. The computed melting times were 25% higher than those obtained by experiments due to some experimental complications, e.g. the gas evolution and variation in melting

temperature were not considered in the model. It was also shown that higher preheating and superheating temperatures and lower melting point of scrap lead to lower melting times.

Szekely et al. [2] developed a mathematical model to study both heat and mass transfer when the carbon content of the melt is higher than the scrap. The heat balance at the scrap – melt interface, used as a boundary condition, was written as:

$$k\frac{\partial T}{\partial r} = h(T_L - T_m) + \rho_p L_p \frac{dr}{dt} \quad (2)$$

where r is radius, ρ_p is the density of the scrap, T_L is the melt temperature, T_m is the melting temperature of the scrap, h is the heat transfer coefficient between melt – scrap, k is the thermal conductivity, and L_p is the latent heat of phase change.

Equation (2) was solved for solid cylinders of different sizes using Green's function [3]. Melting of cylinders was also studied experimentally in an induction furnace. It was shown that, carbon diffusion from melt to scrap facilitates the melting process by lowering the melting temperature of scrap, so the melting temperature of scrap, T_m, was a function of time. Also, Heat transfer coefficient was estimated by fitting the data obtained by the model to the experimental results.

Ehrich et al. [4] studied the melting rate of a single sponge iron sphere in its own melt using both experiments and the same technique used by Szekely et al. [2]. The alumina markers were applied to detect the melting surface for a specific time in a 20 kg induction furnace. The melting curve (radius – time) obtained experimentally was fitted to the one obtained numerically for a constant heat transfer coefficient (31400 W/m^2K). It was shown that an increased melt or initial sphere temperature decreases the melting time and thickness of the initial solidified shell; moreover, it increases the heat transfer coefficient.

Wu and Lacroix [5] offered a two dimensional heat transfer model in which a lump of scrap metal, which was considered as a medium with a constant porosity and occupied the furnace (D=0.4 m) to a specific height, started to melt. The energy conservation equation was solved in the whole furnace. By assuming constant heat transfer coefficients, the temperature distribution in the furnace was depicted for both natural and forced convection. The calculations showed that the melting time is significantly influenced by heat transfer coefficient.

Zhou et al. [6] used a finite difference method to solve the heat conduction equation for melting aluminium scraps. They studied the influence of scrap size and preheating temperature, melt temperature and forced convection on the melting rate. It was shown that agitation in the melt, studied by increasing the Nusselt number, facilitates the melting process. The temperature distribution was obtained during melting of aluminium scraps in a rotary furnace using a three dimensional CFD model, in which only the fluid flow in the gas phase was simulated [7]. Using a discretized population balance model (PBM), scrap size variations were applied, and equation 2 was simplified by neglecting the temperature difference inside the aluminium particles, so the radius changes of scrap was calculated as:

$$dr = -\frac{h(T_L - T_m)}{\rho_p L_p} dt \quad (4)$$

Li et al. [8] investigated the melting process of a number of scrap pieces in an EAF. The experiments showed that the spacing between scrap bars influences melting by formation of solid shells, called steel icebergs. Using the phase field model (PFM) [9], melting of randomly distributed scraps was simulated in two dimensions. It was shown that the high value of the heat transfer coefficient, related to forced convection, resulted in a lower melting time in comparison to conduction dominated melting.

In most of previous works, only the heat conduction equation was solved considering the boundary condition at the solid – liquid interface. Others [5, 6, 7], considered the whole melt as a computational domain, but the heat transfer coefficient was assumed to be constant. In none of previous works [1, 2, 4-9], the fluid flow was simulated in the bath.

Widlund et al. [10] used numerical model to study the effect of electromagnetic stirring on fluid flow, temperature homogenization and mixing efficiency. They showed that using ABB electromagnetic stirrer EMS-EAF, the circulation in the bath is significantly improved leading to an increased temperature homogenization and efficient mixing. In the present work, the same domain and simulation tool are applied to study heat transfer and fluid flow during melting of a single scrap in an electric arc furnace. Both natural convection and electromagnetic stirring (EMS) in the bath are taken into account. Temperature distribution and radius changes of scrap are computed for three different scrap radii, preheating temperatures, force magnitudes and stirring directions; in fact, the objective of this work is to compare the effect of natural convection and EMS on the melting process and to predict the rate of heat flow at the scrap – melt interface obtained by computing heat transfer coefficient.

2. Mathematical Modeling

2.1. Computational Domain

The computational domain is a melt region of a hypothetical 150 t electric arc furnace with eccentric bottom tapping (EBT), **Figure 1 (a)**. The dimensions of the computational domain are listed in **Table 2**. Three arc spots are created using three circles at the top surface of the melt.

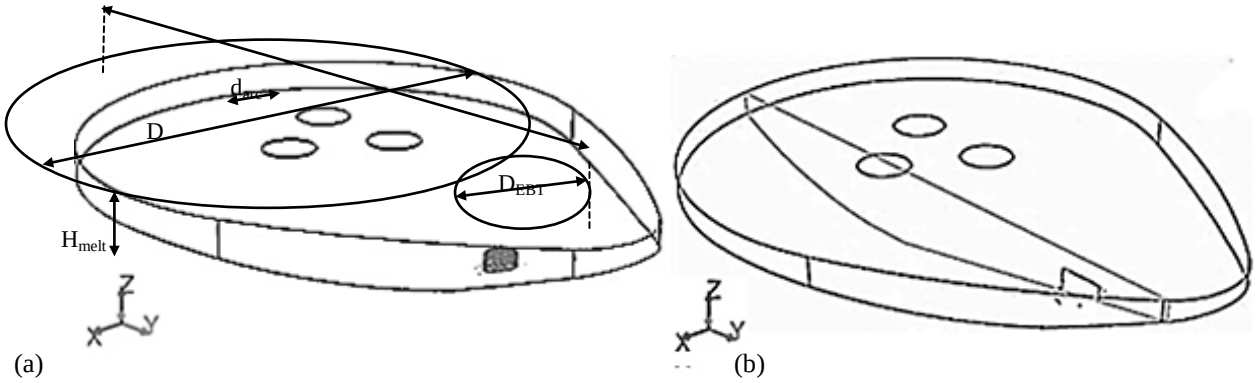

Figure 1. (a) Shape and size of the Computational domain; the scrap (red) modeled in the EBT region; (b) the vertical surface through the center of the scrap.

Table 2. Dimensions of the computational domain.

Parameter	Volume	D	D_{EBT}	H_{melt}	d_{arc}	L_{melt}
Value	22.02	5.7	1.8	1.17	0.6	7.2
Unit	m^3	m	m	m	m	m

The following numerical assumptions are applied:

- Three-dimensional
- Unsteady state condition
- Constant thermodynamic properties
- Scrap with the same properties as the melt (no mass transfer)
- No electromagnetic force due to the arcs, no momentum transfer at the melt surface due to the arc and no gas bubbling inside the melt

2.2. Governing Equations

The continuity and momentum conservation equations and equations for the turbulence model are used to solve the fluid flow problem.

Continuity Equation:

$$\nabla.\left(\rho\vec{V}\right) = 0 \tag{5}$$

where $\vec{V}$ is the velocity vector.

Momentum conservation equation for the case of natural convection:

$$\frac{\partial\left(\rho\vec{V}\right)}{\partial t} + \nabla.\left(\rho\vec{V}\vec{V}\right) = (\rho - \rho_\infty)\vec{g} - \nabla P + \nabla.(\bar{\bar{\tau}}) + S \tag{6}$$

where P is the static pressure, $\bar{\bar{\tau}}$ is the stress tensor, ρ_∞ is the fluid density in ambient medium, and $\vec{g}$ is gravitational acceleration vector. The term $(\rho - \rho_\infty)\vec{g}$ is the buoyancy force, F_b, and S is the momentum source term will be defined in equation 14.

Momentum conservation equation for the case of EMS:

$$\frac{\partial\left(\rho\vec{V}\right)}{\partial t} + \nabla.\left(\rho\vec{V}\vec{V}\right) = (\rho - \rho_\infty)\vec{g} - \nabla P + \nabla.(\bar{\bar{\tau}}) + F + S \tag{7}$$

where F is the electromagnetic (Lorentz) force, added as an external body force.

Equation for the turbulence model: The realizable k– ε eddy viscosity model for high Reynolds numbers proposed by Shih et al. [11] is used to calculate turbulent viscosity. In this model, a new equation for the dissipation rate is recommended in which the dissipation rate is a function of mean square vorticity fluctuations, or mean strain rate, instead of Reynolds stresses.

In this model, a new turbulent viscosity formulation as a function of turbulent kinetic energy, k, and dissipation rate of turbulent kinetic energy, ε, is defined as:

$$\mu_t = C_\mu \frac{k^2}{\varepsilon} \tag{8}$$

where C_μ is a function of mean strain and rotation of the fluid, and it prevents unrealizable values when the mean strain rate is large.

The model coefficients used in this study is based on the results achieved by Shih et al. [11].

Equations for the melting model: For modeling of melting, the enthalpy – porosity technique proposed by Voller et al [12] is employed. In this model, the phase change takes place in cells modeled as a pseudo porous media with the porosity, λ. As the latent heat content, ΔH, decreases from L (fully liquid cell) to 0 (fully solid cell), the porosity decreases from 1 to 0. The mushy zone is referred to the cells in which $0 < \lambda < 1$. The local liquid fraction, F_l, equal to the porosity, is described in solid, liquid and mushy zones as:

$$F_l(T) = \begin{cases} 0 & T < T_{solidus} \\ \dfrac{T - T_{solidus}}{T_{liquidus} - T_{solidus}} & T_{solidus} < T < T_{liquidus} \\ 1 & T > T_{liquidus} \end{cases} \tag{9}$$

The **energy conservation equation** is written as:

$$\frac{\partial(\rho H)}{\partial t} + \nabla.\left(\rho \vec{V} H\right) = \nabla.(k \nabla T) + S_h \tag{10}$$

where H is sum of the sensible enthalpy, h, and the latent heat, $\Delta H = \lambda L$, defined as:

$$h = h_{ref} + \int_{T_{ref}}^{T} C_p \, dT \tag{11}$$

where h_{ref} is the reference enthalpy, T_{ref} is the reference temperature, and C_p is the specific heat capacity, and S_h is the enthalpy source term.

In the enthalpy – porosity technique [12], the momentum source, S, is defined as:

$$S = C \frac{(1-\lambda)^2}{(\lambda^3 + q)} \left(\vec{V}\right) \tag{12}$$

where q is a small number, 0.001 and C is the porosity constant that depends on the morphology of the mushy zone.

2.3. Scrap geometry

A single cylindrical piece of scrap is defined in the EBT region by assuming that all cells inside the cylinder have an initial constant temperature, 300 K, and zero liquid fraction, **Figure 1 (a)**. Three initial radii R=0.1, 0.15 and 0.2 m and cylinder axis length L=0.14 m are used. Grid refinement is applied in the scrap region and 0.1 m around the scrap changing during melting to have a higher resolution mesh and less numerical diffusion.

2.4. Boundary conditions

Bottom and side walls: Bottom and side refractories are assumed as thin walls with specific thickness and thermal resistance, but no thermal inertia. It is assumed that the heat is transferred by conduction across the wall and then convection and radiation to the ambient medium. The no-slip condition is considered for all walls, which means that the melt velocity relative to the wall is zero.

Top, slag: The slag is defined explicitly as a stationary solid wall at the top surface of the melt with the same method used for refractories; however, a high thermal conductivity is assigned for the slag wall to compensate for the convective heat transfer through the slag layer in reality.

Top, arcs: It is assumed that all heat is transferred to the melt through the arc spots, and no heat is dissipated by radiation at the melt surface. The heat flux corresponding to the arc power is used as a boundary condition and added as a source term in equation 10. Moreover, to reach a robust convergence for the case of natural convection, the power is ramped up gradually as three volume sources are assigned at the height of 0.3 m below the arc spots. During the power ramp up, which takes 60 s, the power inside three volumes decreases, and afterwards, the full power is supplied to the melt surface.
The boundary condition parameters are listed in **Table 3**.

Table 3. Boundary condition parameters.

Boundary condition parameter	Value	Unit
Bottom wall thickness, h_{bw}	0.8	m
Side wall thickness, h_{lw}	0.4	m
Slag thickness, h_{slag}	0.25	m
Source height, h_{source}	0.3	m
Ambient temperature	300	K
Freeboard temperature	1000	K
Arc power	50	MW

2.5. Material properties

Physical and thermodynamic properties of steel, slag and refractories are listed in **Table 4**.

Table 4. Steel, slag and refractory properties.

Model parameter	Value	Unit
Steel density	6900	kg/m^3
Steel specific heat capacity	792	J/kg.K
Steel viscosity	0.007	kg/m.s
Steel thermal conductivity	35	W/m.K
Steel thermal expansion	0.0003	1/K
Steel latent heat	240,000	J/kg
Refractory thermal conductivity	0.5	W/m.K
Slag thermal conductivity	80	W/m.K
Heat transfer coefficient outside of refractories	10	$W/m^2.K$
Operating temperature	1800	K

2.6. Calculation procedure

ANSYS FLUENT 13.0.0 is used to solve the conservation equations, and the software VectorFields OPERA, a finite element method (FEM) based solver, is used to compute the electromagnetic forces in a stagnant melt. Thus, when the forces are imported to FLUENT to be added to the momentum equation, a correction is applied to compensate for the melt velocity. As a result, the electromagnetic force in the horizontal stirring direction, y, is computed as:

$$F_y = F_{0,y}\left(1 - \frac{v}{2f\tau}\right) \tag{13}$$

where v is the velocity compensate, f is the stirrer frequency, and τ is the distance between two magnetic pole centers.

In forward stirring, the force is applied towards the EBT region, and in backward, stirring direction is vice versa.

In FLUENT, a user defined function (UDF) is used to initialize the scrap geometry inside the melt, and to model the thermal resistance of the bottom and side refractories, the shell conduction option [13] is applied. The SIMPLE algorithm and PRESTO! scheme are used for the pressure – velocity coupling and pressure discretization respectively. The energy equation is solved after 200 s when a developed flow is established. In the melting model, the porosity or mushy zone constant, C, is set to the default value 10^5 kg/m^{3}s.

A parameter FORCEMAG is assigned as a scaling factor for the electromagnetic volumetric forces. It varies between 0 and 1 corresponding to no stirring and full stirring condition respectively. The values 0.25, 0.5, 0.75 and 1 are used in this study for FORCEMAG, for both forward and backward stirring.

For the case of natural convection, the Boussinesq approximation is applied to solve buoyancy driven flow. In this model, density variation with temperature changes is assumed linear, so in equation 6 and 7, the buoyancy force is written as:

$$F_b = g(\rho - \rho_\infty) = g\rho_b\beta(T - T_\infty) \tag{14}$$

where T_∞ is the operating temperature, β is the thermal expansion, valid for $\beta(T - T_\infty) \ll 1$, and ρ_b is the Boussinesq or reference density of the fluid, given in **Table 4**. To include buoyancy, the gravitational acceleration is applied in z direction, - 9.81 m/s^2.

3. Results and discussion

3.1. Effect of stirring

The middle section through the scrap with R=0.15 m in the melt is used to illustrate the scrap changes and temperature and velocity distribution during melting, **Figure 1 (b)**.

The velocity distribution in the melt is shown in **Figure 2** for both EMS and natural convection. In the later one, **Figure 2 (a)**, the flow descends from the melt surface close to the arc spots towards the lateral walls having lower temperature; then, it flows towards the scrap, with the lowest temperature in the melt, 300 K, and finally it ascends towards the melt surface. The region on the bottom right side of the melt has relatively high velocity magnitude, 0.14 m/s, but still the most part of the

melt is stagnant. With electromagnetic stirring, **Figure 2 (b)**, the flow covers almost the entire bath as more than half of the scrap is disappeared. The high concentration of the velocity arrows around the scrap is due to the mesh refinement. It can be seen that the velocity magnitude around the scrap has increased by about ten times when EMS is applied.

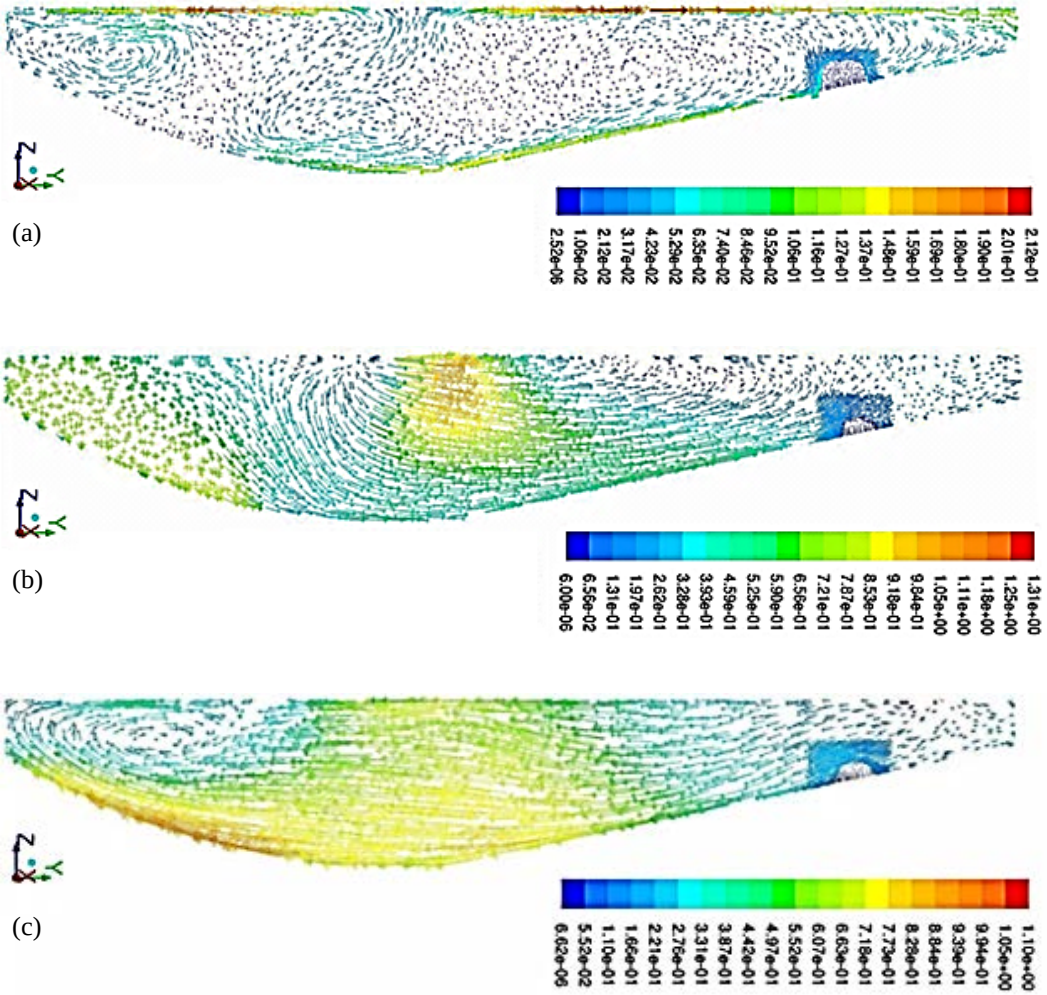

Figure 2. Comparison between velocity distribution of (a) natural convection, (b) forward stirring and (c) backward stirring; after 60 s.

Figure 3. shows temperature distribution for both cases. With only natural convection, strong stratification occurs as three zones are recognized in the melt without including the scrap. This is in good agreement with the works done previously on natural convection in EAF [14, 15]. In contrast, using electromagnetic stirring, temperature is homogenized inside the melt, and the superheated region close to the arc spots disappears. This shows that a strong convective heat transfer is dominant in the melt.

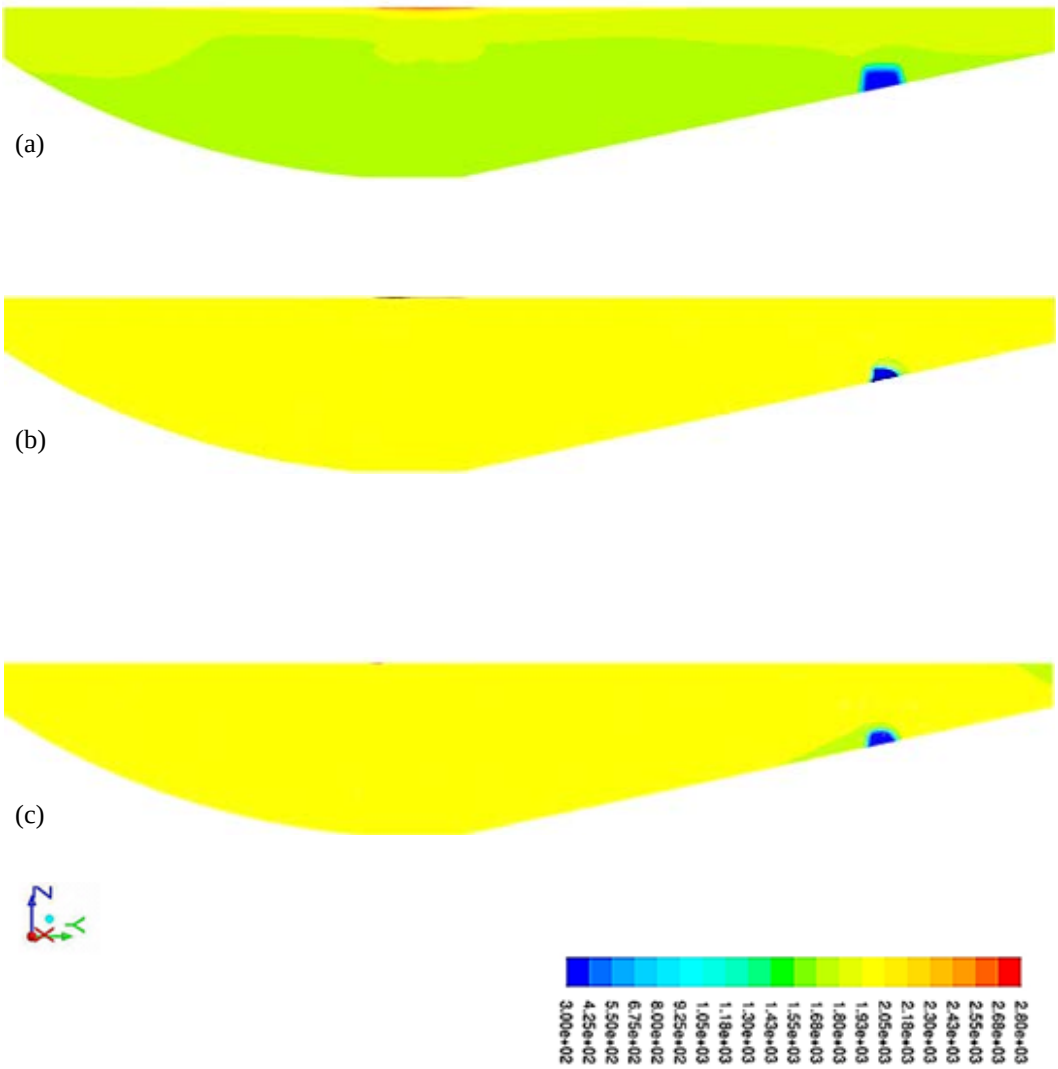

Figure 3. Comparison between temperature distribution of (a) natural convection, (b) forward stirring and (c) backward stirring; after 60 s..

Figure 4 shows the solid region in the melt 60 s after that the heat transfer is started. When only natural convection is present in the melt, the solidified shell is formed around the scrap and reaches to the bottom surface of the furnace, **Figure 4 (a)**. This is also shown more clearly in the cross sectional and top view of the scrap in **Figure 5 (b)** where it is compared to its initial condition, **Figure 5 (a)**. In contrast, when EMS (Forward direction and FORCEMAG=1) is applied, more than half of the scrap is melted after 60 s, **Figure 4 (b)**.

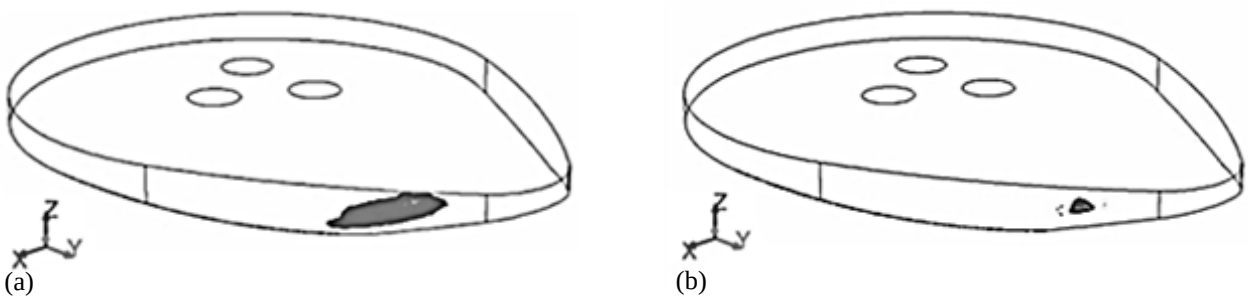

Figure 4. The solid region in the melt for (a) natural convection and (b) electromagnetic stirring; after 60 s.

Aforementioned is shown numerically in **Figure 6** by using volume decreasing of the scrap, expressed by a parameter, *solid remaining* as:

$$Solid\ remaining = \frac{Scrap\ volume_{(t)}}{Scrap\ volume_{(t=0)}} \tag{15}$$

According to **Figure 6**, the melting time is reduced about four times by using EMS, and the formation of the solidified shell is almost omitted.

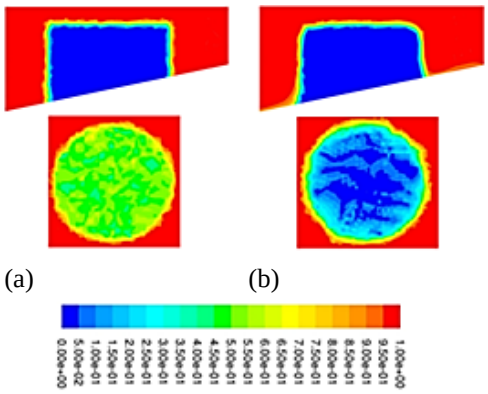

Figure 5. Liquid fraction in the cross sectional and top view of the scrap showing the formation of solidified shell around the scrap; (a) for t=0 and (b) for natural convection for t=18 s.

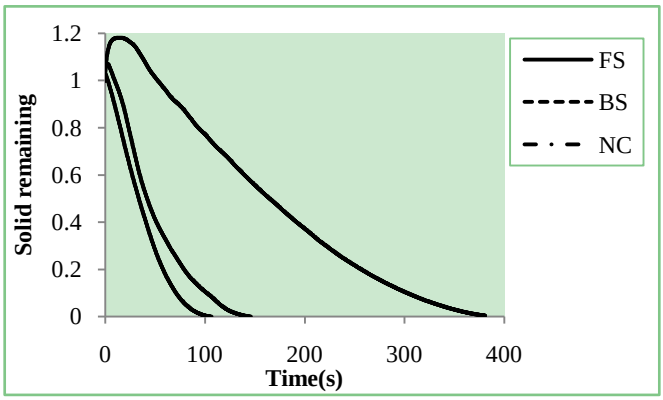

Figure 6. Comparison between natural convection (NC) and backward (BS) and forward stirring (FS)

Figure 7 shows volume averaged velocity inside the melt versus time for backward and forward stirring and natural convection. When electromagnetic stirring is applied, first, melt is accelerated, taking less than 300 s; then for forward stirring, there is a stable velocity fluctuations around 0.5 m/s, while the velocity fluctuations for backward stirring is less stable. For natural convection, the averaged velocity is close to zero.

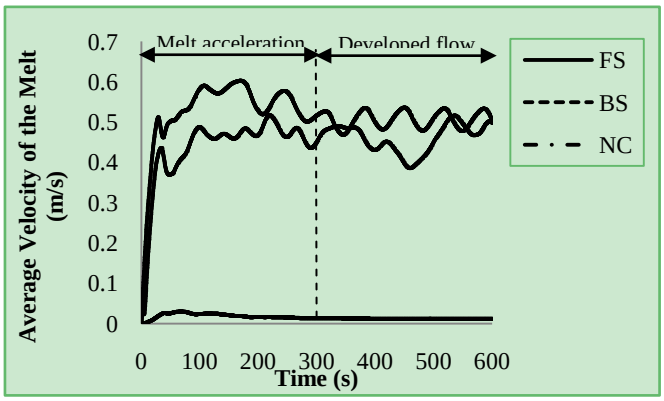

Figure 7. Comparison between velocity of melt for natural convection (NC) and backward (BS) and forward stirring (FS); R=0.15 m.

3.2. Effect of stirring direction

Comparison between velocity distribution for backward and forward stirring after 60 s, **Figure 2 (c)** and **Figure 2 (b)** respectively, shows that applying force towards the EBT region leads to higher velocity magnitude in the melt. The velocity around the scrap varies between 0.16 and 0.22 m/s in forward stirring and between 0.19 and 0.26 m/s in backward stirring. Temperature distribution for forward stirring is more homogenized in forward stirring, **Figure 3 (b)** compared to that for backward stirring, **Figure 3 (c)**. Thus, the melting time is lower when forward stirring is applied, and formation and melting of the solidified shell around the scrap in backward stirring is more significant, **Figure 6**.

3.3. Effect of scrap size and preheating

Figure 8 (a) shows that for the scrap with R=0.1 m, the amount of solid remaining is maximum since the interface area between solid and melt is smaller, and it has the lowest melting time. Volume variations versus time is shown in **Figure 8 (b)**, for three different scrap sizes, and for a period of time from end of the solidified shell melting to the time to reach 0.4 solid remaining, $t_{0.4}$. The slope of the fitted lines can indicate melting rate. It is shown that melting rate for the scrap with R=0.2 m is maximum, 0.0003 m^3/s, which is due to its larger interface area with the melt. **Figure 9** shows that melting time varies with the scrap radius linearly, which is in good agreement with previous works [9].

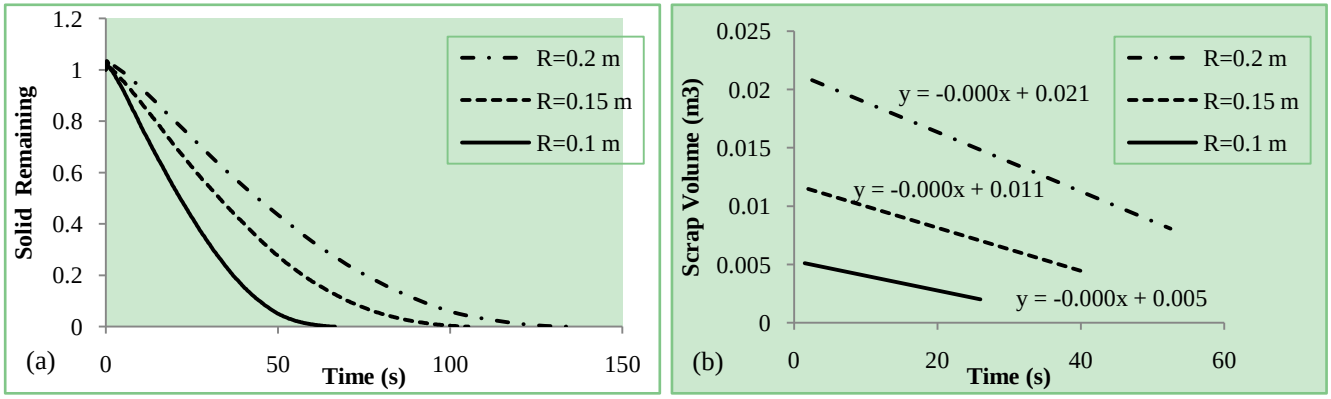

Figure 8 . Comparison between (a) scrap melting and (b) melting rate for 3 different radii.

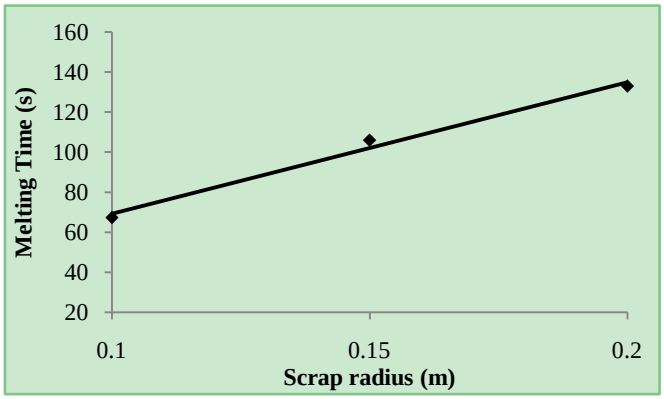

Figure 9. Melting time for different scrap radii.

The effect of preheating temperature on melting time is shown in **Figure 10** indicating that preheating the scrap above room temperature facilitates melting. The correlation between melting time and initial temperature of scrap is linear, **Figure 11**, which is in good agreement with previous works [9].

3.4. Heat transfer coefficient

The minimum temperature versus time for both EMS and natural convection conditions is presented in **Figure 12**. The end time for both is the time to reach 0.2 solid remaining in the melt. It shows that when natural convection is applied, the minimum temperature of scrap increases about 120 K, whereas it is almost unchanged with EMS. This indicates a strong convective heat transfer in the bath and conduction dominated melting resulted by EMS and natural convection respectively.

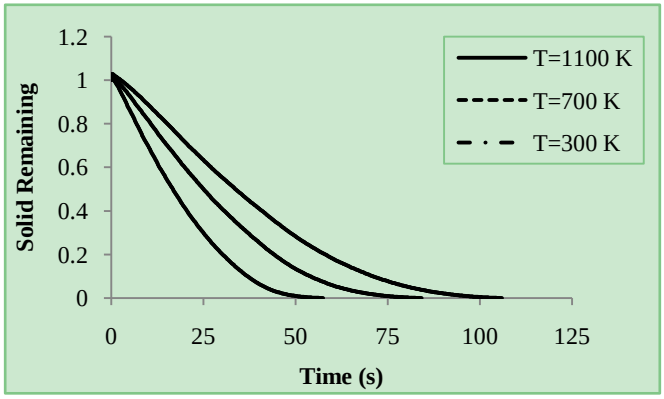

Figure 10. Comparison between melting for three different initial temperatures; R=0.15 m.

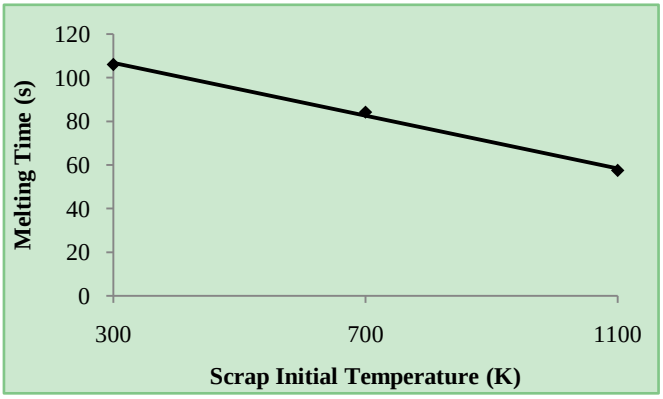

Figure 11. Melting time for different initial scrap temperatures; R=0.15 m.

Consequently, it can be assumed that the temperature difference inside the scrap is zero when EMS is applied. Thus, the equation 4 is used to calculate the heat transfer coefficient between melt and scrap. The melting rate, $\frac{dr}{dt}$, is calculated as:

$$\frac{dr}{dt} = \frac{1}{A}\frac{\Delta V}{\Delta t} \tag{16}$$

where A is the interface area, Δt is the time step equal to 0.25 s, and ΔV is the volume changes of the scrap. Since monitoring of the interface area in each time step is expensive, it is assumed unchanged during melting.

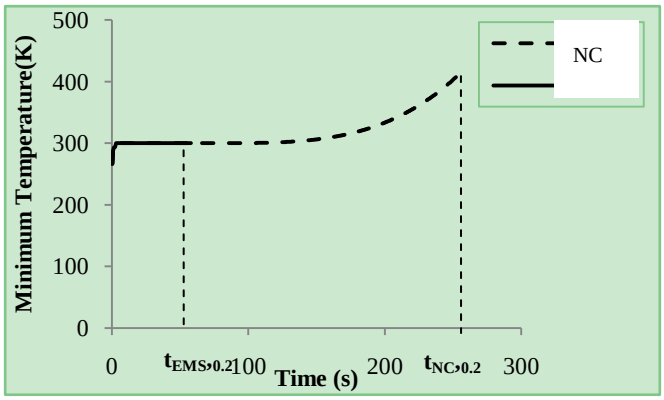

Figure 12. Comparison between minimum temperature for EMS, and natural convection (NC) during the time to reach 0.2 solid remaining in the melt; R=0.15 m.

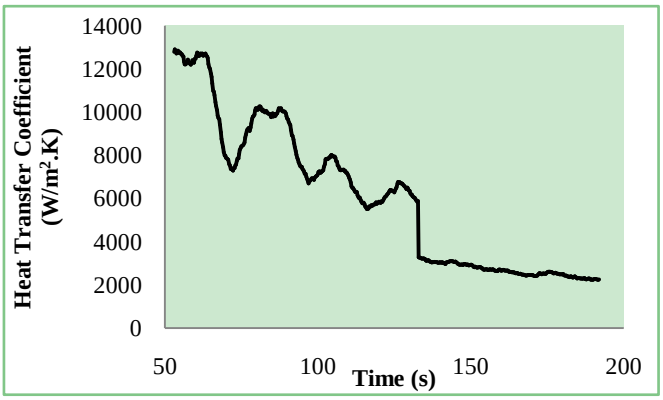

Figure 13. Heat transfer coefficient vs. time to reach 0.4 solid remaining for natural convection; R=0.15 m.

The aforementioned assumption is also applied for natural convection.

The heat transfer coefficient, calculated using equation 4, versus time is shown for natural convection, forward and backward stirring in **Figure 13** and **Figure 14**. The start time is when the solidified shell melted completely, and the end time is the time to reach 0.4 solid remaining.

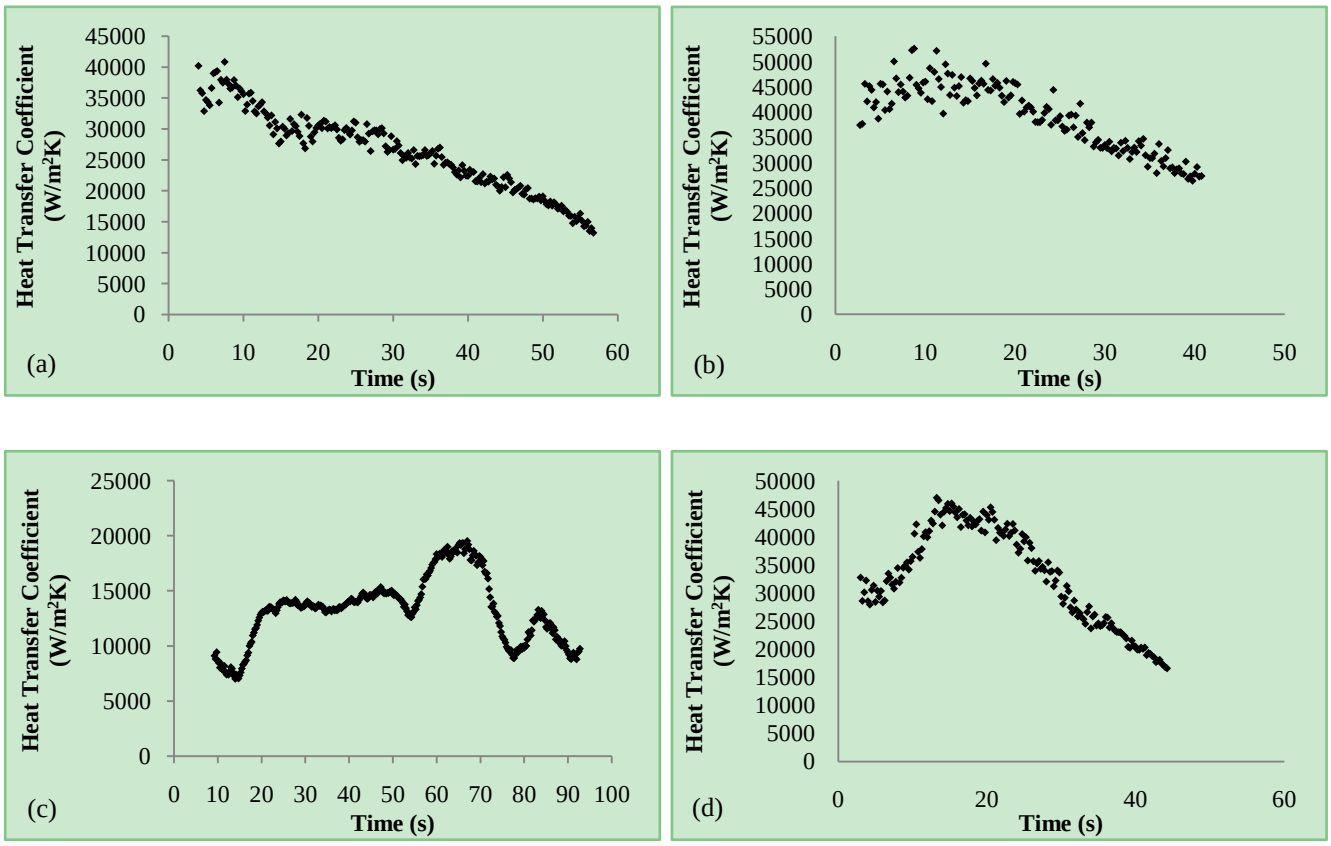

Figure 14. Heat transfer coefficient vs. time to reach 0.4 solid remaining for forward stirring (a) FORCEMAGe=0.25 and (b) FORCEMAG=1 and backward stirring (c) FORCEMAG=0.25and (d) FORCEMAG=1; R=0.15 m.

For natural convection, the heat transfer coefficient varies between 2000-12000 W/m^{2}K. For electromagnetic stirring, the heat transfer coefficient increases with increased force magnitudes. Using forward stirring, the heat transfer coefficient reaches to higher values.

The heat transfer coefficient is a function of melt velocity. For natural convection that the velocity is close to zero, **Figure 7,** the heat transfer coefficient is lower, while using electromagnetic stirring, contributing to higher velocity magnitude in the melt, the heat transfer coefficient increases. The fluctuations of heat transfer coefficient, **Figure 14,** is due to the velocity fluctuation during stirring, **Figure 7**. The heat transfer coefficient decreases for all cases since the interface area is considered unchanged, but in reality it decreases during melting.

The heat transfer coefficient is averaged during the time to reach 0.4 solid remaining, and the time averaged velocity, which is independent of scrap size and temperature, is computed after 600s. The results of average heat transfer coefficient

versus force magnitudes and time averaged velocity are shown in **Figure 15 (a)** and **(b)**. Thus, when the force magnitude or the time averaged velocity is known, the heat transfer coefficient and then the melting time can be predicted.

Although the resolution of mesh in the scrap region is high, numerical diffusion can still exist, which can lead to the higher melting rate.

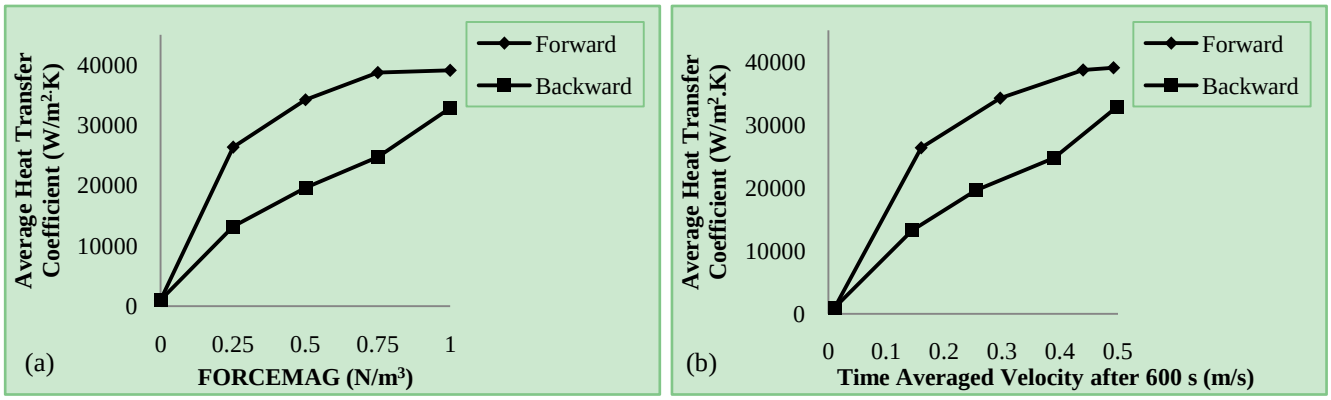

Figure 15. Average heat transfer coefficient vs. (a) force magnitudes and (b) time averaged velocity; after 600s for different force magnitudes; R=0.15 m.

4. Conclusion

The fluid flow, temperature distribution and heat transfer in an EBT EAF were studied numerically considering buoyancy and electromagnetic forces as driving forces for melt circulation. It was observed that using electromagnetic forces, the increased velocity and strong circulation inside the melt contribute to homogenous temperature and lower melting time of the scrap. Furthermore, the heat transfer coefficient was computed and it was shown that it increases by a factor of 4 when electromagnetic stirring is applied

References

[1] R. I. L. Guthrie, L. Gourtsoyannis: *Melting Rates of Furnace or Ladle Additions in Steelmaking*, Canadian Metallurgical Quarterly, 10 (1971), 37 – 46.

[2] J. Szekely, Y. K. Chuang, J. W. Hlinka: *The Melting and Dissolution of Low-Carbon Steels in Iron-Carbon Melts*, Metallurgical Transactions, 3 (1971), 1972 – 2825.

[3] H. S. Carslaw, J. C. Jaeger: *Conduction of Heat in Solids*, Oxford University Press, 1959.

[4] O. Ehrich: *The Melting of Sponge Iron Spheres in Their Own Melt,* Arch. Eisenhuttenwes, 50 (1979), no. 8, 329 – 334.

[5] Y. K. Wu, M. Lacroix: *Numerical Simulation of the Melting of Scrap Metal in a Circular Furnace*, Int. Comm. Heat Mass Transfer, 22 (1995), no. 4, 517 – 525.

[6] B. Zhou, Y. Yang, M. A. Reuter, U. M. J. Boin: *Modelling of Aluminium Scrap Melting in a Rotary Furnace*, Materials Engineering, 19 (2006), 299 – 308.

[7] B. Zhou, Y. Yang, M. A. Reuter: *Modelling of Melting Behaviour of Aluminium Metal in Molten Salt and Metal Bath*, In Proceedings Yazawa International Symposium on Metallurgical and Materials Processing, San Diego, California, USA, 2003, 1249 – 1258.

[8] J. Li, N. Provatas: *Kinetics of Scrap Melting in Liquid Steel: Multipiece Scrap Melting*, Metallurgical and Materials Transactions, 39 B (2008), 268 – 279.

[9] J. Li, G. Brooks, N. Provatas: *Kinetics of Scrap Melting in Liquid Steel*, Metallurgical and Materials Transactions, 36 B (2005), 293 – 302.

[10] O. Widlund, U. Sand, O. Hjortstam, X. Zhang: *Modeling of Electric Arc Furnaces (EAF) With Electromagnetic Stirring*, STEELSIM, 4th International Conference on Modelling and Simulation of Metallurgical Processes in Steelmaking, Düsseldorf, 2011.

[11] T. H. Shih, W. W. Liou, A. Shabbir, Z. Yang, J. Zhu: *A New k-ε Eddy Viscosity Model for High Reynolds Number Turbulent Flows*, Copmuters Fluids, 24(1995), no. 3, 227 – 238.

[12] V. R. Voller, C. Prakash: *A Fixed-Grid Numerical Modeling Methodology for Convection-Diffusion Mushy Region Phase-Change Problems*, Int. J. Heat Mass Transfer, 30 (1987), no.8, 1709 – 1719.

[13] ANSYS FLUENT Theory and User's Guide, Release 13.0.0, 2010.

[14] J. Szekely, J. McKelliget, M. Choudhary: *Heat – transfer fluid flow and bath circulation in electric – arc furnaces and DC plasma furnaces*, Ironmaking and Steelmaking, 10(1983), 169-179.

[15] O. J. P. Gonzalez, M. Ramirez, A. N. Conejo: *Effect of arc length on fluid flow and mixing phenomena in AC electric arc furnaces*, ISIJ International 50(2010), 1 – 8.